Nano Research

Open Access

Research Article

High-current degradation mechanisms in AlGaN deep-ultraviolet LEDs: The role of point defects

Dekun Luo[1], Wei Wu[1], Min Li[1], Qianqian Luo[1], Yaoze Li[1], Ruixing Xue[1], Xuhong Hu[1], Dan Huang[1], Jin Zhong Zhang[2] ✉, Jianyu Deng[1] ✉, Ruosheng Zeng[1], and Wenhong Sun[1] ✉

[1] *Research Center for Optoelectronic Materials and Devices, Guangxi Key Laboratory for the Relativistic Astrophysics, State Key Laboratory of Featured Metal Materials and Life-cycle Safety for Composite Structures, Guangxi Key Metals Research Institute Co., Ltd., Third Generation Semiconductor Industry Research Institute, School of Physical Science and Technology, Guangxi University, Nanning 530004, China*
[2] *Department of Chemistry and Biochemistry, University of California, Santa Cruz, California 95064, USA*

Cite this article: *Nano Research*, **2026**, *19*, 94908952. https://doi.org/10.26599/NR.2026.94908952

ABSTRACT: High-current reliability remains a key factor hindering the commercialization of AlGaN-based deep-ultraviolet light-emitting diodes (LEDs), primarily due to elusive defect-mediated degradation. Here, we investigated the spatial distribution and nature of defects induced by high current stress in 276 nm AlGaN-based LEDs grown on high-quality AlN. The results demonstrate that the stress-induced defects are generated within the p-type layer and the active region, particularly in areas of current crowding. A combined analysis using capacitance–voltage measurements, deep-level transient spectroscopy, and admittance spectroscopy reveals that p-layer degradation is driven by nitrogen vacancy (V_N)-related defects originating from the dehydrogenation of hydrogen-passivated complexes. In the active region, the dominant stress-induced defects are identified as magnesium substituting gallium (Mg_{Ga}), V_N, gallium vacancy (V_{Ga}) complexes, and gallium-nitrogen vacancy (V_{Ga}-V_N) complexes. These defects act as non-radiative recombination centers, enhancing non-radiative recombination and leading to a reduction in optical power. These findings suggest that mitigating hydrogen incorporation and optimizing current spreading are critical to high-current reliability of AlGaN-based deep-ultraviolet LEDs.

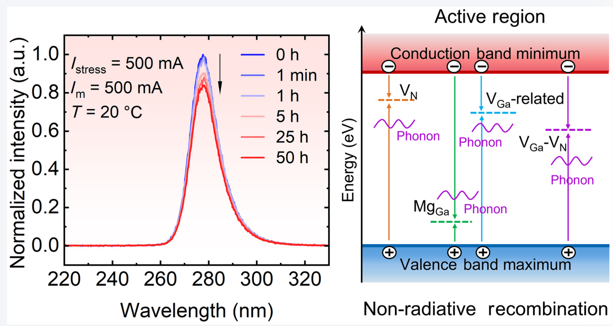

KEYWORDS: AlGaN, degradation, reliability, light-emitting diodes, deep ultraviolet, defect

1 Introduction

AlGaN-based deep-ultraviolet light-emitting diodes (DUV LEDs) (200–280 nm) are expected to become a key alternative to toxic mercury lamps in applications such as disinfection, UV curing, and biochemical sensing, thanks to their compact size, environmental friendliness, and excellent monochromaticity [1–11]. Notwithstanding these advantages, the commercial use of DUV LEDs is severely limited by their lack of operational reliability. Specifically, the higher the current at which DUV LEDs operate, the faster their light output declines. As a result, their operational lifetime is typically limited to a few thousand hours [12, 13]. The root cause of this reliability bottleneck lies in the complex interaction between high-current stress and the dynamic evolution of point defects, which manifests as severe degradation in optical power and an increase in leakage current [14–16].

Due to lattice mismatch, high-aluminum AlGaN alloys are prone to forming various point defects, including cation vacancies, nitrogen vacancies (V_N), and their respective complexes with unintentional impurities [17]. Under high-current stress, these defects may undergo complex diffusion and restructuring processes driven by electron–phonon coupling and local self-heating [18–20]. Previous studies have sought to analyze the degradation mechanisms of AlGaN-based LEDs under electrical stress. Monti et al. suggested that early-stage degradation stems from increased defect density in the final quantum barrier or enhanced carrier escape triggered by positive charge accumulation at the electron blocking layer (EBL) interface, followed by long-term defect diffusion [14]. Similarly, Piva et al. proposed a two-stage model: an initial decline in injection efficiency linked to gallium vacancy

Received: May 8, 2026; **Revised:** June 16, 2026
Accepted: June 17, 2026

✉Address correspondence to Wenhong Sun, 20180001@gxu.edu.cn; Jianyu Deng, ddjy2000@gmail.com; Jin Zhong Zhang, zhang@ucsc.edu

dehydrogenation, and subsequent long-term degradation dominated by deep-level states at 1.6 and 2.15 eV [21]. Despite these insights, our understanding of the types of defects generated under high current stress and their spatial distribution remains incomplete, and further in-depth research is needed.

In this work, we epitaxially grew 276 nm AlGaN DUV LEDs on high-quality AlN and systematically investigated the spatial distribution and nature of defects induced by high-current stress through electrical and optical characterization, deep-level transient spectroscopy, and admittance spectroscopy. The results show that device degradation is more pronounced in areas of current crowding. Furthermore, we identified the types of defects generated in the p-type layer and the active region under high-current stress. The increased defects primarily involve vacancy-related point defects and their complexes. These defects enhance non-radiative recombination and increase leakage current, resulting in a reduction in optical power.

2 Experimental section

2.1 LED fabrication and material characterizations

The AlGaN-based LEDs used in this study were grown on sapphire substrates along the (0001) plane using metal-organic chemical vapor deposition (MOCVD). As shown in Fig. 1(a), a 3 μm AlN layer was first grown on a (0001) sapphire substrate, followed by a transition layer consisting of 20 pairs of AlN/$Al_{0.8}Ga_{0.2}N$. Subsequently, a 1.5 μm Si-doped n-$Al_{0.6}Ga_{0.4}N$ layer was deposited. Thereafter, 5-period $Al_{0.45}Ga_{0.55}N$ (3 nm)/$Al_{0.55}Ga_{0.45}N$ (7 nm) multiple quantum wells (MQWs) were grown. Finally, a 30 nm p-$Al_{0.8}Ga_{0.2}N$ EBL, a 30 nm p-$Al_{0.56}Ga_{0.44}N$ layer, and a 10 nm p-GaN contact layer were grown in sequence. After epitaxial growth, standard chip processing techniques were used to fabricate the device, with Ti/Al and Ni/Au deposited for the n-type and p-type electrodes, respectively. The LED was packaged in a flip–chip configuration, with a single chip size of 1000 μm × 1000 μm and a junction area of 0.65 mm^2.

Epitaxial LED materials were characterized using high-resolution X-ray diffraction (HRXRD) (Malvern Panalytical, X'PERT3 MRD), X-ray photoelectron spectroscopy (XPS) (Thermo ESCALAB 250XI), and atomic force microscopy (AFM) (Shimadzu SPM-9700).

2.2 High-current accelerated aging test for LEDs

A batch of 20 consistent 276 nm DUV LEDs were subjected to accelerated aging at a high current of 500 mA (current density ≈ 77 A/cm^2). To suppress the self-heating induced by high current, the LED was soldered onto a copper printed circuit board (PCB) and mounted on a Peltier-based thermoelectric controller maintained at 20 °C. The LEDs underwent 50 h of aging at a high current of 500 mA, and their optical and electrical properties were characterized at specific time intervals. Optical power and optical power–current (L–I) characteristics were measured using an integrating sphere (ZPL-100UV). Electroluminescence (EL) and photoluminescence (PL) spectra were acquired via Ocean Optics Maya2000 Pro and HORIBA LabRAM HR Evolution, respectively. Current–voltage (I–V) measurements were performed using a Keithley 2400 Source Meter. Capacitance–voltage (C–V) profiling was carried out with a Keysight E4980A LCR meter. To identify defects in the device, admittance spectroscopy (AS) and deep-level transient spectroscopy (DLTS) tests were performed before and after aging. AS was conducted using a LINKAM probe station equipped with a temperature controller in conjunction with the Keysight E4980A LCR bridge. DLTS measurements were performed on a PhysTech FT1030 system.

3 Results and discussion

The high-resolution XRD pattern of the (002) plane of the LED epitaxial wafer is shown in Fig. 1(b). The diffraction peak at 41.67° corresponds to the sapphire substrate. Considering that the diffraction peaks for GaN and AlN are at 34.56° and 36.03°, respectively, it can be inferred from the Vegard's law that the diffraction peak at 35.3° corresponds to n-$Al_{0.6}Ga_{0.4}N$. Due to the thinness of the multi-quantum well layers, the corresponding diffraction peaks are too weak to be resolved. Additionally, XPS was performed to characterize the surface of the LED epitaxial wafer, as shown in Fig. 1(c). Peaks associated with Ga, N, and Mg can be observed in the XPS spectrum, which is consistent with the fact that the surface layer of the LED epitaxial wafer is p-GaN. The entire LED epitaxial structure is based on high-quality AlN grown on a sapphire substrate. Figure 1(d) shows the AFM image of the AlN grown on a sapphire substrate. The AlN surface exhibits a smooth morphology, with a root-mean-square (RMS) roughness of 0.11 nm. We further evaluated the crystal quality of the AlN by X-ray rocking curves, as shown in Figs. 1(e) and 1(f). The full width at half maximum (FWHM) values of the X-ray diffraction rocking curves for the (002) and (102) planes of AlN are 94 and 219 arcsec, respectively, indicating a low dislocation density in the AlN material. The AlGaN material in the LED epitaxial structure grown on this high-quality AlN was characterized by X-ray diffraction rocking curves, presented in Fig. 1(g). The FWHM of the (102) X-ray diffraction rocking curve for AlGaN is 438 arcsec, indicating that the AlGaN material epitaxially grown on this high-quality AlN also exhibits good crystal quality. The DUV LED fabricated from this epitaxial wafer exhibited a peak external quantum efficiency (EQE) of 9.6% at 50 mA and an optical power of 114 mW at 300 mA (Fig. S1 in the Electronic Supplementary Material (ESM)).

To investigate the degradation mechanisms of AlGaN-based DUV LEDs under high current stress, a batch of 20 consistent 276 nm DUV LEDs were subjected to accelerated aging tests at 500 mA and 20 °C. After being subjected to high current stress, the optical power exhibited a monotonically decreasing trend over time at all test currents, as shown in Fig. S2 in the ESM. Figure 2(a) shows the variation of normalized optical power over time as a function of stress time at different test currents. It can be observed that the decay of optical power exhibits two distinct degradation phases. In the early stage (< 5 h), a similar degree of optical power decay was observed across all test currents. However, during long-term stress phases (> 5 h), the decline in optical power at low test current levels is significantly greater than at high current levels. The early degradation of optical power is attributed to a worsening of carrier injection efficiency, as the degradation of optical power is almost independent of the test current [21]. The long-term degradation of optical power is attributed to an increase in non-radiative recombination due to the generation of defects [21]. Figure 2(b) shows the evolution of the EQE as a function of stress time for different test currents. The decrease in external quantum efficiency shows little dependence on the test current in the early stages. However, over the long term, the rate of degradation in

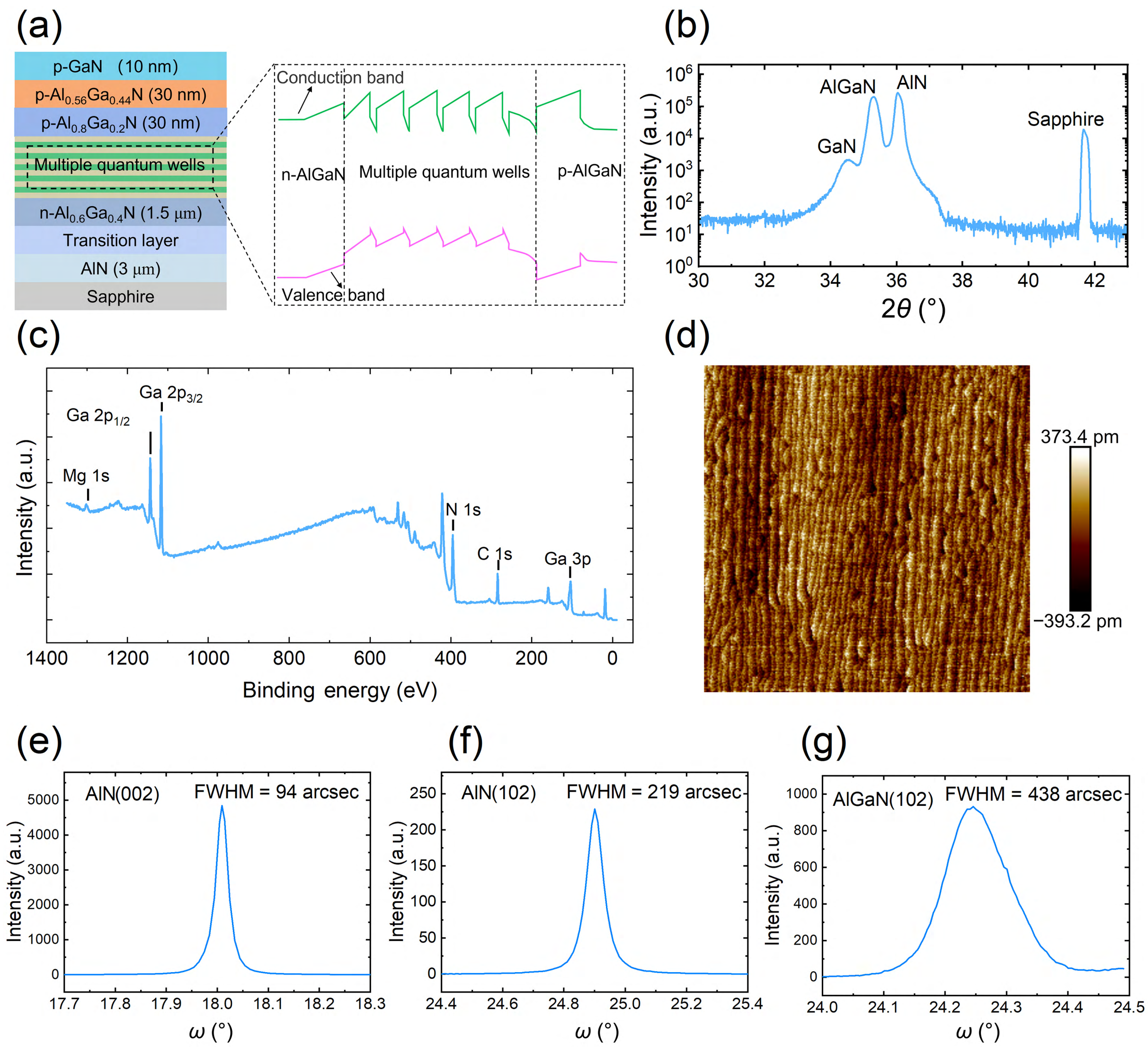

Figure 1 (a) Schematic diagram of the epitaxial structure of the 276 nm deep-ultraviolet LED. (b) XRD 2θ–ω scans of the (002) plane of the entire LED epitaxial structure. (c) X-ray photoelectron spectroscopy of the (002) surface of the entire LED epitaxial structure. (d) AFM image of AlN grown on sapphire. ((e) and (f)) X-ray rocking curves of (e) the (002) and (f) (102) planes of AlN grown on sapphire. (g) X-ray rocking curve of the (102) plane of AlGaN in the LED epitaxial wafer.

external quantum efficiency is much more severe at low test currents than at high test currents. This further indicates a worsening of carrier injection efficiency during the early stages of stress and an increase in non-radiative recombination during long-term stress.

EL measurements were used to study the optical degradation of devices under high current stress. Figure 2(c) shows the electroluminescence spectra under different stress time. It can be observed that the emission intensity of the quantum well (QW) continuously decays without any significant spectral shift. This indicates that the Al content of the quantum well has not changed. Furthermore, PL measurements were performed on the same device before and after aging using a 325 nm laser at room temperature (Fig. 2(d)).

The PL spectrum exhibits enhanced yellow-green emission around 500 nm after stress, which has been attributed to an increase in gallium vacancy-related defects in previous studies [20]. In addition, the brightness distribution on the top and bottom sides of the unaged device in Fig. 2(e) is uneven, indicating uneven current diffusion. After aging, the upper side of the chip shows a more pronounced decrease in brightness, indicating that degradation is more severe in regions of current crowding.

The *I*–*V* characteristics under different stress time are shown in Fig. S3 in the ESM. Both the reverse leakage current (< 0 V) and the low forward leakage current (0–4.5 V) increase with stress time. According to previous literature, the increase in reverse leakage current is attributed to the generation of defects in or around the active region (Fig. S4 in the ESM), which form parasitic current paths [22]. Meanwhile, the enhancement of trap-assisted tunneling (TAT) leads to an increase in the low forward leakage current [22]. In the high-injection regime (> 5.5 V), transport is governed by the series resistance (R_s), as shown in Figs. S3(c) and S3(d) in the ESM. R_s decreases during the early stage (< 5 h), which is attributed to the dehydrogenation of Mg-H complexes (activation of Mg acceptors) [23]. This is further confirmed by the corresponding reduction in the driving voltage (Fig. S5 in the ESM). Subsequently, R_s gradually increases during the long-term stage, likely due to the degradation of the p-contact [24].

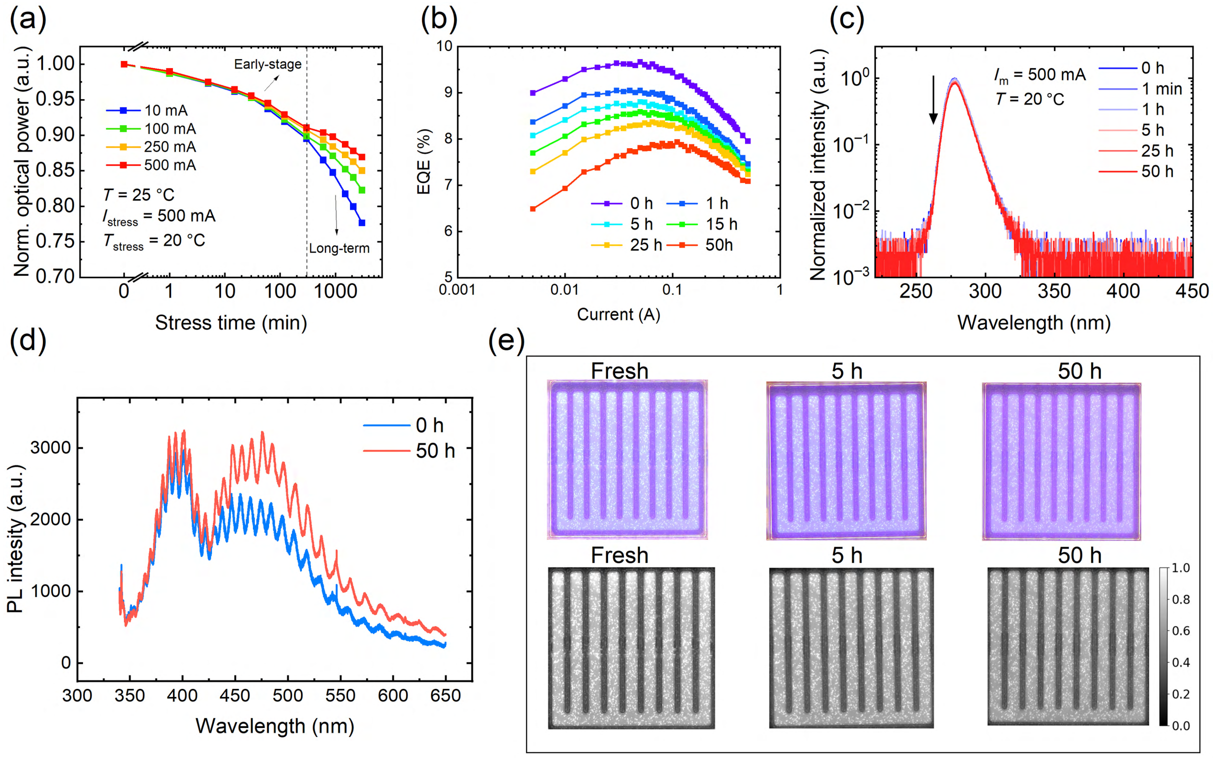

Figure 2 (a) The normalized optical power as a function of stress time at various test currents. (b) EQE variation as a function of current at different stress time. (c) EL spectra at different stress time measured at a current of 500 mA. (d) PL spectra of devices before and after stress under 325 nm laser excitation. (e) Electroluminescence images of the device at 250 mA test current changing with stress time (250 mA stress) and corresponding reprocessed images.

C–V measurements at various test frequencies were performed to analyze the spatial distribution and capture kinetics of stress-induced defects (Figs. S6(a)–S6(c) in the ESM). It can be observed that the capacitance shows significant variation above 1 MHz, while only slight variation is seen below 1 MHz. This difference suggests that current stress may induce defects with different energy-level depths in these regions. The apparent carrier distribution (ACD) and depletion width (W) were extracted using Eqs. (1) and (2)

$$N_{\mathrm{B}}(W) = \frac{2}{q\varepsilon_0\varepsilon_{\mathrm{r}}A^2}\left[-\frac{1}{\mathrm{d}(1/C^2)/\mathrm{d}V}\right] \tag{1}$$

$$W = \frac{A\varepsilon_0\varepsilon_{\mathrm{r}}}{C} \tag{2}$$

where N_{B} represents the carrier concentration, q is the electron charge, ε_{r} and ε_0 are the relative permittivity and vacuum permittivity, respectively, A is the junction area, V is the test voltage, and C is the capacitance [25]. The ACD profiles reveal peaks corresponding to the QWs, ranging from the last quantum well (LQW) near the p-side to the first quantum well (FQW) near the n-side (Figs. S6(d)–S6(f) in the ESM). It can be observed that after current stressing, the carrier concentration in the three quantum wells near the p-side increases significantly, indicating that the newly generated defects are predominantly located close to the p-side. Notably, the depletion width at high frequency (> 1 MHz) narrows during the early stage (< 5 h) and subsequently widens. The initial narrowing is attributed to an increase in the effective Mg acceptor concentration within the electron blocking layer [26]. Meanwhile, the depletion width at low frequency (< 1 MHz) remains nearly unchanged. This may be due to the dehydrogenation of hydrogen-passivated deep-level donor-like defects in the p-type layer (likely cation-nitrogen-vacancy clusters, e.g., V_{III}-V_{N}) [27, 28], which compensates the charge from the activated Mg acceptors. After 25 h, the increase in depletion width at 2 MHz indicates a reduction in the net acceptor concentration, which is likely due to dislocation-assisted Mg diffusion into the active region [29, 30]. This corresponds to the increase in series resistance.

To definitively identify the stress-induced deep-level defects, deep-level transient spectroscopy (DLTS) was performed before and after aging (Figs. 3(a) and 3(b)), targeting two distinct zones: region 1 (forward bias, 2–4.5 V) and region 2 (reverse bias, −6–−11 V), as shown in Fig. S7 in the ESM. Figure 3(a) shows the DLTS signal spectrum of region 1. After 50 h of stress, the peaks of the majority carrier trap E_1 and the minority carrier trap H_1 both increased, accompanied by the appearance of a new electron trap E_2. As shown in Fig. S8 in the ESM, their activation energy (E_{a}) was obtained from the Arrhenius plot. The activation energy of defect E_1 is 0.16–0.19 eV (capture cross section: from 7.59×10^{-20} to 1.19×10^{-20} cm^2; defect concentration: from 3.79×10^{17} to 7.69×10^{17} cm^{-3}). The activation energy of defect H_1 is 0.20–0.25 eV (capture cross section: from 6.97×10^{-19} to 1.42×10^{-17} cm^2; defect concentration: from 9.94×10^{17} to 2.62×10^{18} cm^{-3}). The activation energy of defect E_2 is 0.87 eV (capture cross section: 1.02×10^{-14} cm^2; defect concentration: 3.52×10^{16} cm^{-3}). According to previous studies, defect E_1 is a defect associated with V_{N} [31], while defect H_1 is attributed to magnesium substitution at gallium sites ($\mathrm{Mg_{Ga}}$) [32]. The increase in defect H_1 concentration supports the migration of Mg from the p-type layer into the active region, which is consistent with previous studies concluding that Mg migrates along dislocations under electrical stress [29, 30, 32]. The migration of Mg in the p-type layer leaves behind gallium vacancies. The PL data

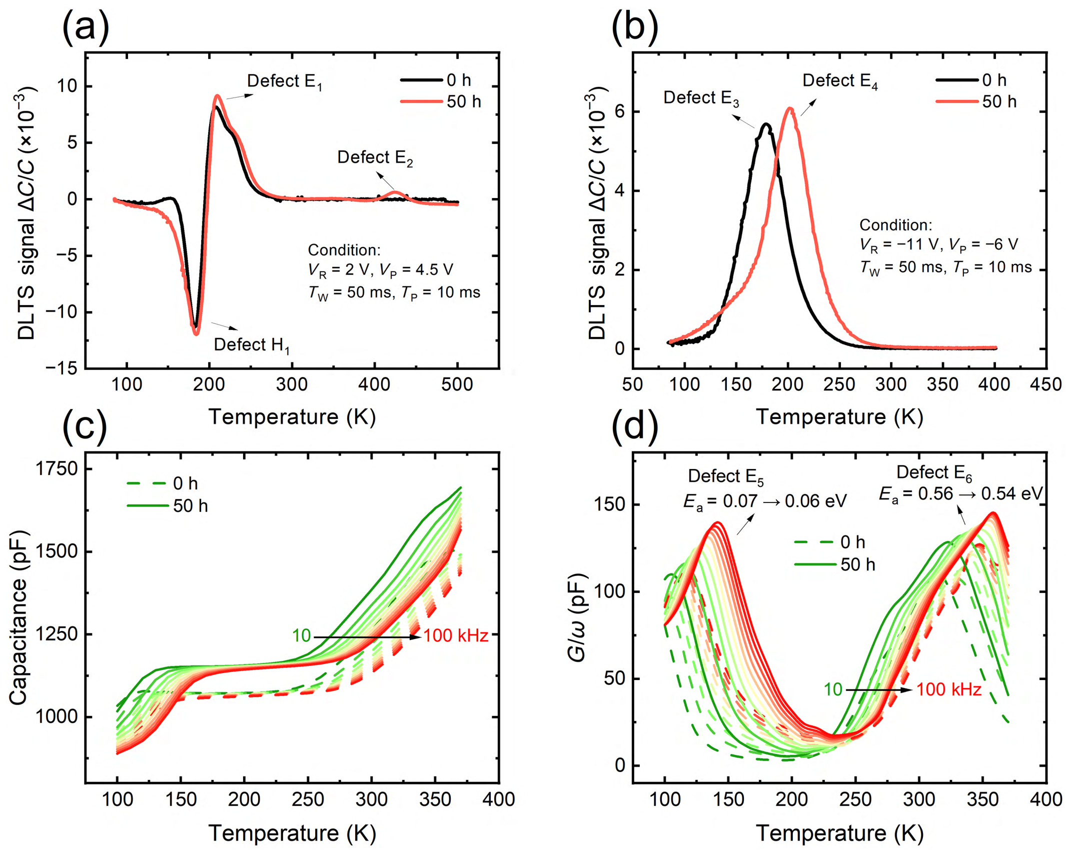

Figure 3 ((a) and (b)) DLTS signal spectroscopy in (a) region 1 and (b) region 2 before and after aging. In our DLTS measurement system, positive and negative peaks are associated with majority carriers (electrons) and minority carriers (holes), respectively. ((c) and (d)) Temperature dependence of (c) capacitance and (d) G/ω before and after stress, with frequencies ranging from 10 to 100 kHz.

corroborate the increase in the concentration of gallium vacancy-related defects in the p-type layer due to Mg migration. Defect E_2 is considered to be a gallium-nitrogen vacancy (V_{Ga}-V_N) complex [33]. We propose that Mg migration leaves behind gallium vacancies, which subsequently complex with V_N. In region 2, DLTS spectra exhibit a single majority-carrier trap that evolves from defect E_3 in the pristine state to defect E_4 after aging (Fig. 3(b)). The activation energy shifts significantly from 0.33 to 0.50 eV (capture cross section: from 4.53×10^{-15} to 5.13×10^{-12} cm^2; defect concentration: from 2.55×10^{17} to 3.11×10^{17} cm^{-3}). According to the report by Huang et al., the energy level at 0.33 eV was identified as a nitrogen-vacancy-related defect on the AlGaN surface [34]. Similarly, defect E_3 discussed here can be identified as a nitrogen vacancy-related defect. Previous studies have reported that the energy level of gallium vacancy-related defects is approximately 0.5 eV [20], and the energy level of Mg-V_N complex defects is between 0.4 and 0.5 eV [35]. Since no previous studies have reported V_N-V_{Ga}-related defect levels around 0.5 eV, and based on our inference of Mg migration into the active region, we now consider defect E_4 most likely to be a Mg-V_N complex defect. Therefore, the evolution of defect E_3 (0.33 eV) to E_4 (0.50 eV) is most probably due to Mg migrating from the p-type layer into the active region under electrical stress and subsequently forming Mg-V_N complex defects with existing V_N-related defects.

To probe shallow-level defects beyond the DLTS detection limit, admittance spectroscopy was performed. Capacitance–frequency (C–f) curves under different stress time were recorded at 4 V (Fig. S9 in the ESM), corresponding to the depletion of the last quantum well as identified by apparent charge distribution profiles. The temperature dependence of capacitance and G/ω (where G is the ac conductance, ω is the angular frequency, and $\omega = 2\pi f$) at various frequencies are shown in Figs. 3(c) and 3(d), respectively. In these two graphs, each curve represents data measured at a different test frequency. The test frequency ranges from 10 to 100 kHz with a step size of 10 kHz, and the temperature scan step is 10 K. In Fig. 3(d), each peak represents the presence of a type of defect. The temperature-dependent G/ω resolve two distinct peaks, defect E_5 and defect E_6. The Arrhenius plot can be calculated from the peak temperatures corresponding to different frequencies shown in Fig. 3(d). For defect E_5, the temperature range employed to extract data for the Arrhenius plot was 110–150 K; for defect E_6, it was 310–360 K. The activation energies of defects E_5 and E_6 before and after aging were extracted from the Arrhenius plot. For defect E_5, the values are 0.07 and 0.06 eV, respectively; for defect E_6, they are 0.56 and 0.54 eV, respectively (Fig. S10 in the ESM). Based on literature, defect E_5 is identified as a nitrogen vacancy-related defect, and defect E_6 as a gallium vacancy-related complex [20, 36]. In addition, the energy level of defect E_6 is similar to that of defect E_4 in DLTS, suggesting that they are the same type of defect. The increase in the peak after stress indicates a rise in the concentration of nitrogen-vacancy and gallium-vacancy related defects.

The nature of defects in the active region of LEDs was investigated using first-principles calculations based on density functional theory (DFT) [37–39]. We modeled a 108-atom $Al_{0.5}Ga_{0.5}N$ supercell containing Mg substitution for Ga and nitrogen vacancy, as shown in Figs. 4(a)–4(c). To allow for a direct

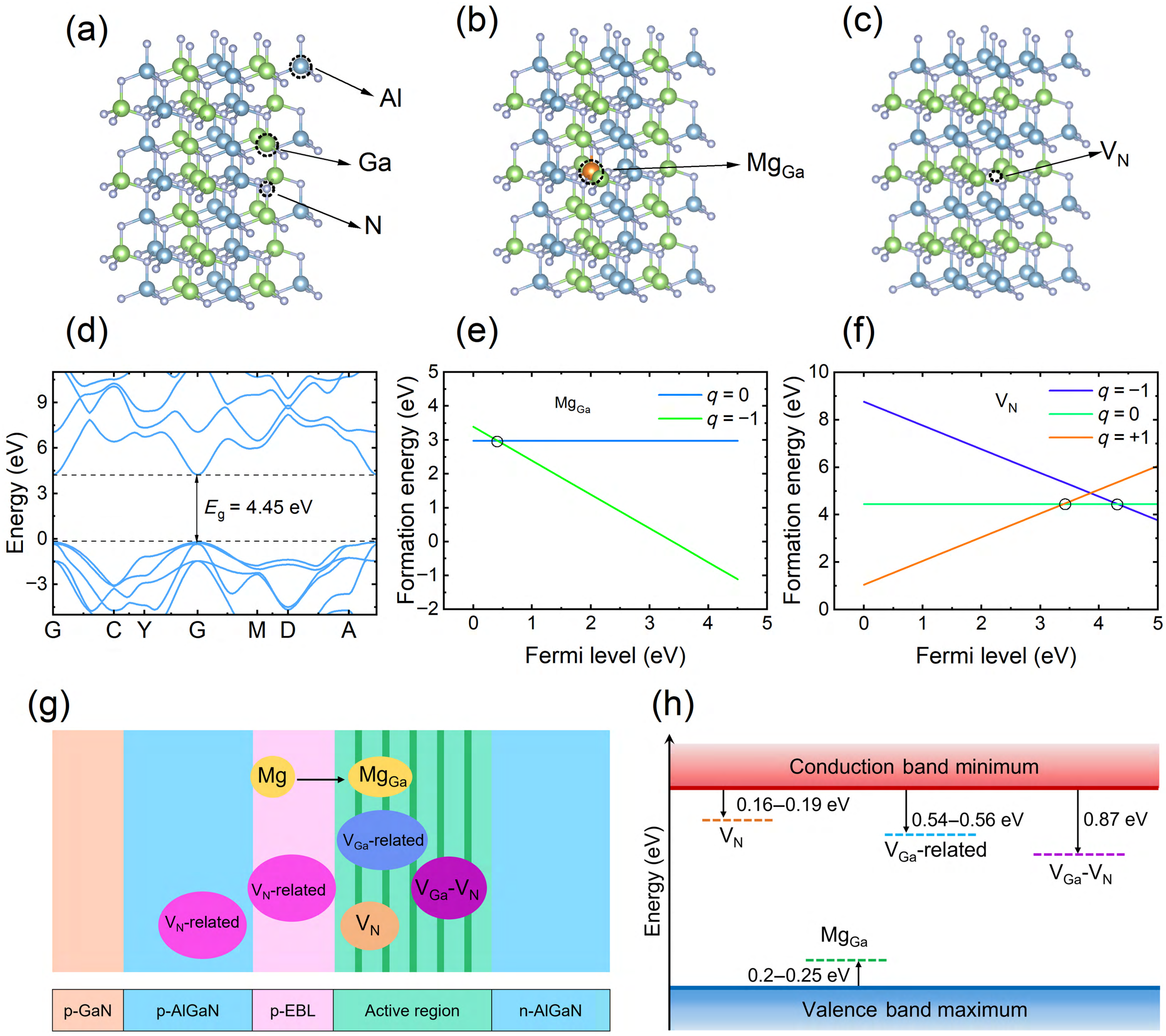

Figure 4 ((a)–(c)) The 3 × 3 × 3 $Al_{0.5}Ga_{0.5}N$ supercell models include: (a) the perfect supercell, (b) Mg substituting for Ga, and (c) a nitrogen vacancy. (d) Band structure diagram of the $Al_{0.5}Ga_{0.5}N$ unit cell. (e) Formation energy of Mg_{Ga} as a function of fermi energy under metal-rich conditions. (f) Formation energy of V_N as a function of fermi energy under metal-rich conditions. (g) Schematic diagram of the defect evolution mechanism in AlGaN-based DUV LEDs induced by high current stress. (h) Schematic diagram of the energy levels of deep-level defects induced by high current stress in the active region.

comparison with the DLTS data, we calculated the thermodynamic transition levels, $E(q/q')$, which represent the critical Fermi-level positions where a defect undergoes a transition between different charge states. The calculated bandgap of 4.45 eV (Fig. 4(d)) aligns well with the theoretical value (4.5–4.64 eV) [40]. Figures 4(e) and 4(f) present the formation energies under metal-rich conditions. The calculated (0/−1) transition level for Mg_{Ga} lies 0.41 eV above the valence band maximum (E_v). This is slightly higher than the DLTS result (0.2–0.25 eV) and experimental reports (~ 0.3 eV) [41], a discrepancy likely attributed to finite-size effects in the supercell which overestimate the doping concentration. For V_N, the (+1/0) and (0/−1) transitions occur at 3.4 and 4.3 eV above the valence band maximum, corresponding to depths of 1.05 and 0.15 eV below the conduction band minimum (E_c), respectively. Notably, the (0/−1) level at E_c − 0.15 eV is in excellent agreement with the DLTS signal (0.16–0.19 eV).

Based on the preceding analysis, the location and evolution mechanism of defects induced by high current stress can be determined, as shown in Fig. 4(g). Initially, electrical stress induces the dehydrogenation of hydrogen-passivated V_N complexes within the p-type layer. The increased nitrogen vacancy-related defects compensate for the Mg acceptor, thereby reducing the carrier injection efficiency. Subsequently, the stress induces an accumulation of Mg_{Ga}, V_N, V_{Ga}-related complexes, and V_{Ga}-V_N complexes in the active region. These defects together enhance Shockley–Read–Hall (SRH) non-radiative recombination and increase leakage current. Figure 4(h) maps the deep-level defects within the active region bandgap. V_N, V_{Ga}-related complexes, and V_{Ga}-V_N complexes are positioned at E_c − 0.19, E_c − 0.56, and E_c − 0.87 eV, respectively, while Mg_{Ga} levels are located at E_v + 0.25 eV. To extend the operational lifetime of AlGaN-based DUV LEDs, mitigating hydrogen incorporation is paramount. For instance, employing intense localized electric fields induced by chloride ions for hydrogen extraction has proven to be an effective strategy [42].

4 Conclusions

In summary, we systematically investigated the spatial distribution and nature of defects induced by high-current stress in 276 nm AlGaN DUV LEDs grown on high-quality AlN. Electrical stress induces the formation of defects in the p-layer and the active region, particularly in areas of current crowding. Specifically, electrical stress triggers the dehydrogenation of hydrogen-passivated nitrogen-vacancy complexes in the p-layer, leading to the formation of V_N-related defects. Synergistic analysis using DLTS, admittance spectroscopy, and density functional theory calculations identifies the predominant active-region defects as Mg_{Ga}, V_N, V_{Ga} complexes, and V_{Ga}-V_N complexes, characterized by activation energies of 0.25, 0.19, 0.56, and 0.87 eV, respectively. These defect species facilitate non-radiative recombination and exacerbate leakage current. Our findings underscore that reducing hydrogen incorporation and optimizing current spreading are pivotal for improving the reliability of AlGaN-based DUV LEDs under high-current operation.

Electronic Supplementary Material: Supplementary material (first-principles calculations, and additional data, including *I*–*V* characteristics, *C*–*V* characteristics, ideality factor, driving voltage, etc.) is available in the online version of this article at https://doi.org/10.26599/NR.2026.94908952.

Data availability

All data needed to support the conclusions in the paper are presented in the manuscript and the Electronic Supplementary Material. Additional data related to this paper may be requested from the corresponding author upon request.

Acknowledgements

This work was supported by the National Natural Science Foundation of China (No. 62575079), the Guangxi Science and Technology Major Project (No. AA23073018), the High luminous efficiency and long life DUV LED technology (No. AC22080003), the National Key R&D Program of China (No. 2022YFB3605101), the Guangxi Science and Technology Innovation Platform Program (Leitai Action Plan, No. Guike LT2600640026), Guangxi Key R&D Program (Guangxi Funeng Action Plan, No. FN2504240040), the "Guangxi Highland of Innovation Talents" Program, and the Production Development of Epitaxial Wafers Grown by MOCVD (No. KY03000031224002).

Declaration of competing interest

All the contributing authors report no conflict of interests in this work. Author Ruosheng Zeng is the editorial board member of this journal, but he is not involved in the peer-review or decision of this article.

Author contribution statement

D. K. L.: Data curation, validation, writing manuscript, experimental design. W. W., M. L., Q. Q. L., Y. Z. L., R. X. X., X. H. H., and D. H.: Validation, resources, formal analysis. J. Z. Z., J. Y. D., and R. S. Z.: Writing – review & editing, supervision. W. H. S.: Project administration, funding acquisition, writing – review & editing. All the authors have approved the final manuscript.

Use of AI statement

None.

References

[1] Kneissl, M.; Seong, T. Y.; Han, J.; Amano, H. The emergence and prospects of deep-ultraviolet light-emitting diode technologies. *Nat. Photonics* **2019**, *13*, 233–244.

[2] Zhou, S. J.; Liao, Z. F.; Sun, K.; Zhang, Z. Q.; Qian, Y. Z.; Liu, P. F.; Du, P.; Jiang, J. J.; Lv, Z. X.; Qi, S. L. High-power AlGaN-based ultrathin tunneling junction deep ultraviolet light-emitting diodes. *Laser Photonics Rev.* **2024**, *18*, 2300464.

[3] Liu, X.; Lv, Z. X.; Liao, Z. F.; Sun, Y. C.; Zhang, Z. Q.; Sun, K.; Zhou, Q. X.; Tang, B.; Geng, H. S.; Qi, S. L. et al. Highly efficient AlGaN-based deep-ultraviolet light-emitting diodes: From bandgap engineering to device craft. *Microsyst. Nanoeng.* **2024**, *10*, 110.

[4] Li, D. B.; Jiang, K.; Sun, X. J.; Guo, C. L. AlGaN photonics: Recent advances in materials and ultraviolet devices. *Adv. Opt. Photonics* **2018**, *10*, 43–110.

[5] Wu, W. L.; Liu, S.; Liu, Z. Y.; Zhou, X. Y.; Yang, X.; He, X. Y.; Xia, Q. L.; Zhong, M. Z.; Li, J. B.; He, J. High-voltage-resistant wafer-scale 4H-SiC ultraviolet photodetector with high uniformity enabled by electric field distribution modulation. *Nano Res.* **2025**, *18*, 94907259.

[6] de Abajo, F. J. G.; Hernández, R. J.; Kaminer, I.; Meyerhans, A.; Rosell-Llompart, J.; Sanchez-Elsner, T. Back to normal: An old physics route to reduce SARS-CoV-2 transmission in indoor spaces. *ACS Nano* **2020**, *14*, 7704–7713.

[7] Fu, S. H.; Xia, D. Y.; Fu, R. P.; Wang, Y. F.; Han, Y. R.; Gao, C.; Cui, W. Z.; Li, B. S.; Fu, Z. D.; Shen, S. et al. Enhanced ultra-narrowband fast response ultraviolet photodetector based on GaN homojunction with a carbon-doped semi-insulating intermediate layer. *J. Phys. Chem. Lett.* **2025**, *16*, 2681–2689.

[8] Dong, J. Q.; Zhang, D. Q.; Ma, Y.; You, D. T.; Chen, J. P.; Liu, B.; Wang, X. F.; Shi, Z. L.; Xu, C. X. Plasmon-enhanced self-powered GaN/ZnTe core/shell nanopillar array photodetector. *Nano Res.* **2024**, *17*, 5569–5577.

[9] Liu, L. B.; Yin, Z. S.; Lu, X. Y.; Wang, H. C.; Ye, J.; Zhang, Y. Y.; Zhou, C. L.; Shi, J. S.; Luo, J.; Wang, X. L. Light-converting microneedle patch for cutaneous UV phototherapy in psoriasis with enhanced safety and efficiency. *Nano Res.* **2025**, *18*, 94907424.

[10] Wu, Y. Z.; Guo, P. Y.; Luo, D. K.; Deng, J. Y.; Yao, H. L.; Sun, W. H. Feasibility analysis of inactivating influenza A(H1N1) virus using UVC robot in classroom environment. *Heliyon.* **2024**, *10*, e29540.

[11] Lu, Z. H.; Tahir, M.; Yuan, S. X.; Yu, X. X.; Cao, Y. W.; Li, L. H. Fully printed flexible solar-blind self-powered photodetector based on atomic-thin wide bandgap heterostructure. *Nano Res.* **2025**, *18*, 94907698.

[12] Onushkin, G.; Ruschel, J.; Piva, F.; Buffolo, M.; Rass, J.; Davis, L.; Trivellin, N.; De Santi, C.; van Driel, W.; Meneghini, M. Efficiency- and lifetime-limiting effects of commercially available UVC LEDs: A review. *J. Phys. Photonics* **2025**, *7*, 032002.

[13] Zhang, Z. Q.; Zhou, S. J.; Liao, Z. F.; Jiang, J. J.; Geng, H. S.; Lv, Z. X.; Liu, X.; Qi, S. L.; Liu, S. AlGaN polarized ultrathin tunneling junction deep ultraviolet light-emitting diodes. *Nano Lett.* **2025**, *25*, 1898–1906.

[14] Monti, D.; De Santi, C.; Da Ruos, S.; Piva, F.; Glaab, J.; Rass, J.; Einfeldt, S.; Mehnke, F.; Enslin, J.; Wernicke, T. et al. High-current stress of UV-B (In)AlGaN-based LEDs: Defect-generation and diffusion processes. *IEEE Trans. Electron Devices* **2019**, *66*, 3387–3392.

[15] Liu, N. Y.; Wang, Q.; Li, B.; Wang, J. J.; Zhang, K.; He, C. G.; Wang, L.; Song, L. G.; Cao, X. Z.; Wang, B. Y. et al. Point-defect distribution and transformation near the surfaces of AlGaN films grown by MOCVD. *J. Phys. Chem. C* **2019**, *123*, 8865–8870.

[16] Piva, F.; Pilati, M.; Buffolo, M.; Roccato, N.; Susilo, N.; Hauer Vidal, D.; Muhin, A.; Sulmoni, L.; Wernicke, T.; Kneissl, M. et al.

Degradation of AlGaN-based UV-C SQW LEDs analyzed by means of capacitance deep-level transient spectroscopy and numerical simulations. *Appl. Phys. Lett.* **2023**, *122*, 181102.

[17] Ge, L. B.; Tao, R.; Zhang, D. G.; Li, C. H.; Peng, D. Q.; Lu, Y. L.; Li, Z. H. First-principles study of point defects in AlGaN: Insights into defect properties and growth optimization. *Comput. Mater. Sci.* **2025**, *258*, 114054.

[18] Su, M. W.; Liu, H. X. Effect of trap behavior on recombination in AlGaN-based UV-C LEDs degradation. *IEEE Trans. Electron Devices* **2024**, *71*, 1974–1979.

[19] Ma, Z. H.; Almalki, A.; Yang, X.; Wu, X.; Xi, X.; Li, J.; Lin, S.; Li, X. D.; Alotaibi, S.; Al Huwayz, M. et al. The influence of point defects on AlGaN-based deep ultraviolet LEDs. *J. Alloys Compd.* **2020**, *845*, 156177.

[20] Wang, Y. Z.; Wang, M. S.; Hua, N.; Chen, K.; He, Z. M.; Zheng, X. F.; Li, P. X.; Ma, X. H.; Guo, L. X.; Hao, Y. Effects of electrical stress on the characteristics and defect behaviors in GaN-based near-ultraviolet light emitting diodes. *Chin. Phys. B* **2022**, *31*, 068101.

[21] Piva, F.; De Santi, C.; Deki, M.; Kushimoto, M.; Amano, H.; Tomozawa, H.; Shibata, N.; Meneghesso, G.; Zanoni, E.; Meneghini, M. Modeling the degradation mechanisms of AlGaN-based UV-C LEDs: From injection efficiency to mid-gap state generation. *Photonics Res.* **2020**, *8*, 1786–1791.

[22] Monti, D.; Meneghini, M.; De Santi, C.; Meneghesso, G.; Zanoni, E.; Glaab, J.; Rass, J.; Einfeldt, S.; Mehnke, F.; Enslin, J. et al. Defect-related degradation of AlGaN-based UV-B LEDs. *IEEE Trans. Electron Devices* **2017**, *64*, 200–205.

[23] Ma, Z. H.; Cao, H. C.; Lin, S.; Li, X. D.; Zhao, L. X. Degradation and failure mechanism of AlGaN-based UVC-LEDs. *Solid-State Electron.* **2019**, *156*, 92–96.

[24] Shen, C. H.; Yang, R. L.; Gong, H. L.; Zhu, L. H.; Gao, Y. L.; Chen, G. L.; Chen, Z.; Lu, Y. J. Optical power degradation mechanisms in 271 nm AlGaN-based deep ultraviolet light-emitting diodes. *Opt. Express* **2023**, *31*, 20265–20273.

[25] Barnes, P. A. Capacitance–voltage (*C*–*V*) characterization of semiconductors. *Charact. Mater.* **2002**, *1*, 456–466.

[26] Zhu, X. L.; Su, M. W.; Chen, Z. Q.; Deng, S. D.; Yao, H. L.; Wang, Y. K.; Chen, Z. Q.; Deng, J. Y.; Sun, W. H. Degradation analysis with characteristics and simulations of 265 nm UV-C LED. *J. Mater. Sci.: Mater. Electron.* **2021**, *32*, 17115–17122.

[27] Van de Walle, C. G. Interactions of hydrogen with native defects in GaN. *Phys. Rev. B* **1997**, *56*, R10020–R10023.

[28] Chichibu, S. F.; Nagata, K.; Oya, M.; Kasuya, T.; Okuno, K.; Ishiguro, H.; Saito, Y.; Takeuchi, T.; Shima, K. Operation-induced degradation mechanisms of 275-nm-band AlGaN-based deep-ultraviolet light-emitting diodes fabricated on a sapphire substrate. *Appl. Phys. Lett.* **2023**, *122*, 201105.

[29] Lee, S. N.; Paek, H. S.; Son, J. K.; Kim, H.; Kim, K. K.; Ha, K. H.; Nam, O. H.; Park, Y. Effects of Mg dopant on the degradation of InGaN multiple quantum wells in AlInGaN-based light emitting devices. *J. Electroceram.* **2009**, *23*, 406.

[30] Wang, Y. Z.; Zheng, X. F.; Zhu, J. D.; Xu, L. L.; Xu, S. R.; Liang, R. L.; Dai, J. N.; Li, P. X.; Zhou, X. W.; Mao, W. et al. Degradation in AlGaN-based UV-C LEDs under constant current stress: A study on defect behaviors. *Appl. Phys. Lett.* **2020**, *116*, 203501.

[31] Fang, Z. Q.; Look, D. C.; Kim, W.; Fan, Z.; Botchkarev, A.; Morkoç, H. Deep centers in n-GaN grown by reactive molecular beam epitaxy. *Appl. Phys. Lett.* **1998**, *72*, 2277–2279.

[32] Li, M.; Su, M. W.; Chen, Z. Q.; Deng, S. D.; Zhu, X. L.; Zheng, G.; Yang, Y. F.; Wu, W.; Deng, J. Y.; Sun, W. H. Defect behavior on the degradation of AlGaN-based 234 nm LEDs. *IEEE Trans. Electron Devices* **2024**, *71*, 1102–1108.

[33] Reshchikov, M. A.; Morkoç, H. Luminescence properties of defects in GaN. *J. Appl. Phys.* **2005**, *97*, 061301.

[34] Huang, S.; Wang, X. H.; Liu, X. Y.; Kang, X. W.; Fan, J.; Yang, S.; Yin, H. B.; Wei, K.; Zheng, Y. K.; Wang, X. L. et al. Revealing the positive bias temperature instability in normally-OFF AlGaN/GaN MIS-HFETs by constant-capacitance DLTS. In *31st International Symposium on Power Semiconductor Devices and ICs (ISPSD)*, Shanghai, China, 2019, pp 411–414.

[35] Kaufmann, U.; Kunzer, M.; Maier, M.; Obloh, H.; Ramakrishnan, A.; Santic, B.; Schlotter, P. Nature of the 2.8 eV photoluminescence band in Mg doped GaN. *Appl. Phys. Lett.* **1998**, *72*, 1326–1328.

[36] Look, D. C.; Reynolds, D. C.; Hemsky, J. W.; Sizelove, J. R.; Jones, R. L.; Molnar, R. J. Defect donor and acceptor in GaN. *Phys. Rev. Lett.* **1997**, *79*, 2273–2276.

[37] Wu, J.; Chang, T.; Yang, Z.; Zan, H. Z.; Bai, Y. L.; Han, X. X.; Luo, N. N.; Yuan, M. J.; Zeng, R. S. Magneto-chiroptical hybrid perovskites with anomalous photovoltaic effect for high-performance self-driven photodetectors. *Adv. Mater.* **2025**, *37*, 2509074.

[38] Wu, J.; Lin, F. P.; Zhang, S.; Wang, H. Y.; Yao, J. D.; Shen, X. D.; Luo, N. N.; Huang, D.; Zeng, R. S. One-dimensional organic–inorganic hybrid double perovskites with near-unity photoluminescence quantum yield and advanced multifunctional applications. *Chem. Mater.* **2024**, *36*, 3851–3860.

[39] Wang, Y.; Yang, D. Y.; Xu, W.; Xu, Y. J.; Zhang, Y.; Cheng, Z. X.; Wu, Y. Z.; Gan, X. T.; Zhong, W.; Liu, Y. et al. Room-temperature ferromagnetism and piezoelectricity in metal-free 2D semiconductor crystalline carbon nitride. *Nano Res.* **2024**, *17*, 5670–5679.

[40] Oussaifi, Y.; Said, A.; Ben Fredj, A.; Debbichi, L.; Ceresoli, D.; Said, M. Effect of pressure on the energy band gaps of wurtzite GaN and AlN and electronic properties of their ternary alloys $Al_xGa_{1-x}N$. *Phys. B: Condens. Matter* **2012**, *407*, 3604–3609.

[41] Hasan, M. S.; Mehedi, I. M.; Reza, S. M. F.; Kaysir, M. R.; Islam, M. R. Analytical investigation of activation energy for Mg-doped p-AlGaN. *Opt. Quant. Electron.* **2020**, *52*, 348.

[42] Lu, S. Q.; Zhong, Z. B.; Guo, B.; Chen, X. H.; Liu, G. Z.; Lin, Z. F.; Chen, H.; Huang, S. R.; Liang, X. D.; Zheng, Y. Z. et al. Unidirectional elimination of hydrogen by a giant local field saves first-and last-mile performances of semiconductor devices. *J. Phys. Chem. Lett.* **2022**, *13*, 2084–2093.